Modeling of Antenna-Coupled Si MOSFETs in the Terahertz Frequency Range

Florian Ludwig, Jakob Holstein, Anastasiya Krysl, Alvydas Lisauskas, *Member, IEEE*, and Hartmut G. Roskos

***Abstract*—We report on the modeling and experimental characterization of Si complementary metal-oxide-silicon (CMOS) detectors of terahertz radiation based on antenna-coupled field-effect transistors (TeraFETs). The detectors are manufactured using Taiwan semiconductor manufacturing company (TSMC's) 65-nm technology. We apply two models—the TSMC RF foundry model and our own advanced design system (ADS)-hydrodynamic transport model (HDM)—to simulate the Si CMOS TeraFET performance and compare their predictions with respective experimental data. Both models are implemented in the commercial circuit simulation software keysight ADS. We find that the compact model TSMC RF is capable to predict the detector responsivity and its dependence on frequency and gate voltage with good accuracy up to the highest frequency of 1.2 THz covered in this study. This frequency is well beyond the tool's intended operation range for 5G communications and 110-GHz millimeter wave applications. We demonstrate that our self-developed physics-based ADS-HDM tool, which relies on an extended 1-D HDM and can be adapted readily to other material technologies, has high predictive qualities comparable to those of the foundry model. We use the ADS-HDM to discuss the contribution of diffusive and plasmonic effects to the THz response of Si CMOS TeraFETs, finding that these effects, while becoming more significant with rising frequency, are never dominant. Finally, we estimate that the electrical noise-equivalent power (perfect power coupling conditions) is on the order of 5 pW/$\sqrt{\text{Hz}}$ at room-temperature.**

***Index Terms*—Antenna simulation, detection, Gaussian beam, hydrodynamic, MOSFET, power coupling, Taiwan semiconductor manufacturing company (TSMC), terahertz (THz).**

I. Introduction

ANTENNA-COUPLED field-effect transistors (TeraFETs) have emerged as powerful devices for a variety of terahertz (THz) applications such as frequency multiplication and mixing [1], [2], [3], [4], [5], [6], as well as direct THz power detection [1], [7], [8], [9], [10], [11], [12], [13], [14], [15], [16], [17], [18], [19]. The detectors can be readily integrated in electronic circuits and provide sufficient sensitivity at room temperature, which makes them well suited for applications. Among these, TeraFETs fabricated in Si complementary metal-oxide-silicon (CMOS) technology have reached impressive performance levels [13], [20] with a high sensitivity over almost the entire THz frequency range. With the growing variety of possible applications of field-effect transistors (FETs) in the THz range, the need for reliable design and modeling platforms for such devices has increased significantly. Here, we focus on detector simulation and experimentally validate our results. In [21], we presented our simulation approach for TeraFETs—acronym: ADS-HDM. The ADS-HDM is implemented into the circuit simulation environment Keysight advanced design system (ADS)—an industry standard. Its implementation is based on an extended version of the 1-D hydrodynamic transport model (HDM), which has been used in [1]. The frequency-dependent channel impedance is determined from the self-consistent solution of the HDM equations. This physics-based model accounts for the mixing process in the FET channel involving the charge-carrier density waves (plasma waves). They are excited by the incident THz radiation via an antenna element, which couples the radiation asymmetrically to the FET channel, either via the source-gate or the drain-gate port [13], [22], [23], [24], [25]. The evidence for the existence of plasma waves (which are overdamped in the case of Si CMOS at room temperature) has been strengthened by experimental findings described in [23], [26], [27], and [28]. In this work, we present and discuss two simulation approaches to simulate the detector performance of Si CMOS TeraFETs, our in-house tool ADS-HDM as well as the Taiwan semiconductor manufacturing company (TSMC) radio frequency (RF) foundry model (TSMC RF). Prior to the simulations we propose an approach to determine the exact THz input power present at the transistor terminals when the detector is illuminated with a Gaussian intensity profile. The model predictions are compared quantitatively with the optical voltage responsivity determined between 0.4 and 1.2 THz and put into perspective with simulation results obtained with the TSMC RF. The ADS-HDM tool allows to switch the plasmonic effects ON and OFF. Using this feature, we quantify the plasmonic contribution to the THz detector responsivity. Finally, we discuss the upper sensitivity limits of the 65-nm Si CMOS TeraFETs.

II. Hydrodynamic Model Description

In order to simulate the excitation of density waves of the charge carriers in the channel of the Si MOSFET detectors, we

Manuscript received 19 November 2023; revised 15 February 2024 and 22 March 2024; accepted 9 April 2024. Date of publication 12 April 2024; date of current version 3 May 2024. This work was supported by DFG RO under Grant 770/40-1, Grant 770/40-2, Grant 770/43-1, and Grant 770 49-1. *(Corresponding author: Hartmut G. Roskos.)*

Florian Ludwig, Jakob Holstein, Anastasiya Krysl, and Hartmut G. Roskos are with the Physikalisches Institut, Johann Wolfgang Goethe-Universität, DE-60438 Frankfurt am Main, Germany (e-mail: roskos@uni-frankfurt.de).

Alvydas Lisauskas is with the Institute of Applied Electrodynamics and Telecommunications, Vilnius University, LT-10257 Vilnius, Lithuania, and also with the Physikalisches Institut, Johann Wolfgang Goethe-Universität, DE-60438 Frankfurt am Main, Germany.

Color versions of one or more figures in this article are available at https://doi.org/10.1109/TTHZ.2024.3388254.

Digital Object Identifier 10.1109/TTHZ.2024.3388254

use the following 1-D hydrodynamic transport equations:

$$\partial_t n = \frac{1}{q}\partial_x j \tag{1a}$$

$$\partial_t j = \frac{q^2 n}{m^*}E_x + \frac{qk_BT_L}{m^*}\partial_x n + \frac{1}{q}\partial_x\left(\frac{j^2}{n}\right) - \frac{j}{\tau_p} \tag{1b}$$

consisting of the continuity (1a) and the momentum balance (1b), both written in terms of the current density $j = -qnv$, where q is the electron charge, $n = n(x)$ represents the carrier sheet density in the FET's inversion layer along the channel (x-direction), and $v = v(x)$ stands for the local mean carrier velocity. Note that—contrary to the model presented in [1] and [22], the second term on the right-hand side of (1b) also takes carrier diffusion into account. Other quantities of the equations are the longitudinal electric field $E_x = -\partial_x\varphi$ as determined by the channel potential $\varphi(x)$, the electron effective mass ($m^* = 0.26\,m_0$ for electrons in Si in units of the free-electron mass m_0), and the momentum relaxation time τ_p of the electrons. The temperature of the crystal lattice is assumed to be room temperature ($T_L = 293$ K). k_B denotes the Boltzmann constant. The dependence of $n(x)$ on the externally applied gate voltage is taken into account by the unified charge control model (UCCM) for n-channel MOSFETs [29]

$$n(x) = \frac{C_{ox}\gamma U_{th}}{q}\cdot\ln\left(1+\frac{1}{2}\exp\left(\frac{U_{gc}(x)-U_T}{\gamma U_{th}}\right)\right) \tag{2}$$

where $C_{ox} = \frac{\epsilon_R\epsilon_0}{d}$ is the channel capacitance per unit area for a thickness d of the gate insulator. For d, we assume a value of 3.05 nm.[1] $\epsilon_R = 3.9$ is the relative permittivity of the gate insulator, and ϵ_0 the vacuum permittivity. U_T and $U_{th} = \frac{k_BT_L}{q}$ are the threshold voltage and the thermal voltage, respectively. γ represents a nonideality factor, which determines the subthreshold slope of the drain current with regards to the gate-to-source voltage U_{GS}. The gate-to-channel voltage $U_{gc}(x) = U_{GS} - \varphi(x)$ is given by the difference of U_{GS} and the channel potential $\varphi(x)$, the latter being determined self-consistently by jointly solving (1a), (1b), and (2).

The numerical evaluation of this set of equations is performed in the circuit simulation environment of Keysight ADS using a novel distributed-element method approach to integrate the transport equations as presented in [21] for AlGaN/GaN HEMTs. The steady-state solution is obtained by the harmonic balance technique. A schematic of the ADS-HDM implementation is shown in Fig. 1(a). A significant advantage of this simulation approach versus recently developed TCAD models for the THz frequency range [31], [32], [33], [34] is that in the case of circuit based models, such as ADS-HDM [21] or recently developed compact SPICE models [35], [36], extrinsic and parasitic device components are readily included in the full simulation domain [as indicated in Fig. 1(a)], while for TCAD simulations they have to be included via more complex mixed mode simulation methods [37]. At the same time, the full physical model for the description of the plasma-wave mixing process in the transistor's channel is retained at the model's core (hydrodynamic domain). By manipulating or switching OFFindividual terms in (1a), (1b), and (2), one can study and identify the influences of the various physical processes included in the equations.

A number of input values for the parameters of the simulations, as presented in Table I, can be obtained from the measured dc drain-to-source resistance (see below). This makes it easier to test whether variations of the THz performance of each TeraFET

[1]Note that the value of d represents an effective insulator thickness. $d = d_{\text{phys}} + d_{qc}$ is the sum of the physical insulator thickness ($d_{\text{phys}} = 2.6$ nm) and a quantum correction of $d_{qc} = 0.45$ nm arising from the quantum-confinement effect of electrons at the Si-to-SiO_2 interface in nanoscale MOSFETs [30]. The value of $d_{\text{phys}} = 2.6$ nm is taken from the information sheet of the 65-nm CMOS foundry process.

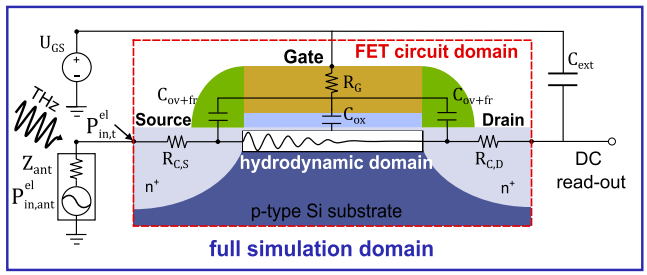

(a)

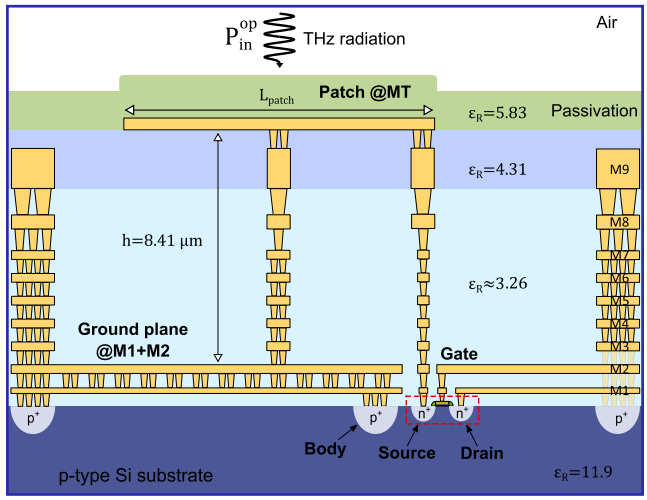

(b)

Fig. 1. (a) Schematic of the ADS-HDM simulation tool: blue box (full simulation domain) represents the THz detector model (is taken in the same manner for the TSMC RF foundry model), here for source radiation coupling conditions. At its core (hydrodynamic domain), the hydrodynamic transport equations are used to calculate the rectified signal of the detector on the basis of plasma-wave-modified resistive mixing in the transistor's channel. The equations are solved in the keysight ADS simulator itself. The FET parasitics are taken into account in the FET circuit domain. Parasitic components considered are the source and drain overlap C_{ov} and fringe capacitances C_{fr}, the contact resistances $R_{C,S}$ and $R_{C,D}$, and the gate resistance R_G. The antenna parameters including the antenna impedance Z_{ant} are estimated from EM wave simulations (CST studio suite). For details of the HDM implementation, we refer to [21]. (b) Cross-sectional view of the detector implementation in TSMC 65-nm process. The patch antenna is implemented underneath a passivation layer in the top metal layer MT. The ground plane is placed in lowest to metal layers M1 and M2.

TABLE I
EXTRACTED SIMULATION PARAMETERS FOR THE ADS-HDM OF THE DIFFERENT SI CMOS TERAFETS OBTAINED THROUGH A FITTING MODEL BASED ON THE UCCM

Device (Patch length)	W (μm)	τ_p (fs)	U_T (V)	γ	R_C (Ω)	μ ($\frac{\text{cm}^2}{\text{Vs}}$)
A1 (130 μm)	1	19.14	0.45	1.9	36.37	129.48
A2 (122 μm)	1	19.67	0.456	1.89	61.25	133.09
A3 (84 μm)	1	18.84	0.474	2.22	63.5	127.44
A4 (58 μm)	0.45	20.38	0.454	2.56	82.46	137.85

may be caused by fabrication-related issues, which also affect the dc device properties.

III. 65-nm Si CMOS TeraFETs

The detectors studied in the following are designed for a commercial 65-nm CMOS foundry process (CLN65LP, type 1.2V_mLow_Vt_MOS) of the TSMC. Fig. 1(b) displays a cross-sectional schematic view of the detector design. In brief, a narrow-band rectangular patch antenna, which is placed in the last metal layer M10, collects the THz radiation and guides the signal through a via at one of the narrow sides of the patch to the source of a single transistor placed directly under the edge of the patch. The height of the patch above the ground plane (metal layer M1 and M2) is $8.41\ \mu$m.

In the following, four different devices are studied with respect to their detector performance. The devices differ only in terms of their respective patch length L_{patch} [see micrograph with the values in Fig. 2(a)], which results in different resonant frequencies. The patch width is fixed to 40 μm. A 1.3-μm-thick passivation layer covers the devices. An important figure of merit, which determines the efficiency of our detectors, is the optical voltage responsivity $\mathcal{R}_V^{\text{op}}$.[2] It is defined as the rectified voltage (or current) signal between the drain and source terminal ΔU_{DS} with regards to the available optical THz input power $P_{\text{in}}^{\text{op}}$, the total power of the incident THz beam in free-space [38], [39]

$$\mathcal{R}_V^{\text{op}} = \frac{\Delta U_{\text{DS}}}{P_{\text{in}}^{\text{op}}}. \tag{3}$$

In this work, the responsivity is measured with the help of an optoelectronic spectroscopy system [TeraScan 1550, Toptica Photonics AG, Graefelfing (Munich)], where the optoelectronic detector is replaced by our TeraFETs. ΔU_{DS} is measured using the lock-in technique. For this purpose, the bias to the photoconductive emitter is modulated with a sine wave at $f_{\text{mod}} = 7.62$ kHz. A schematic drawing of the measurement setup is displayed in Fig. 6(a). Continuous-wave THz radiation between 0.1 and 1.2 THz is generated by an InGaAs photomixer emitter. Its radiation is guided to the Si CMOS TeraFET via four off-axis paraboloid (OAP) mirrors with 90°-beam-deflection geometry. The THz beam path is purged by dry nitrogen in order to minimize radiation absorption by water vapor. The total power $P_{\text{in}}^{\text{op}}$ of the incoming THz beam in front of the Si CMOS TeraFET, placed in the focal point of the last OAP mirror, is measured using a calibrated large-area Golay cell.

The peak-to-peak rectified voltage between drain and source contacts is obtained as $\Delta U_{\text{DS}} = \alpha_{\text{LIA}} \cdot U_{\text{LIA}}$, where U_{LIA} is the lock-in amplifier's output signal. It is proportional to the rms of the first Fourier fundamental component of the detector signal. α_{LIA} represents a lock-in correction factor. For an ideal sinusoidal modulation (e.g., by electronic chopping) of an emitter, the lock-in correction factor is found to be a constant value of $\alpha_{\text{LIA,corr}} = 2\sqrt{2}$. However, inspection with an oscilloscope shows that the THz wave is not modulated sinusoidally, but rather exhibits a more square-wave-like waveform with a detailed shape, which depends on the beat-note frequency of the laser radiation. Measured results and the derivation of the THz-frequency-dependent values of $\alpha_{\text{LIA,corr}}$ are discussed in Appendix A. $\alpha_{\text{LIA,corr}}$ is found to increase linearly with frequency from ~ 2.4 (at 0.1 THz) to ~ 3.1 (at 1.2 THz).

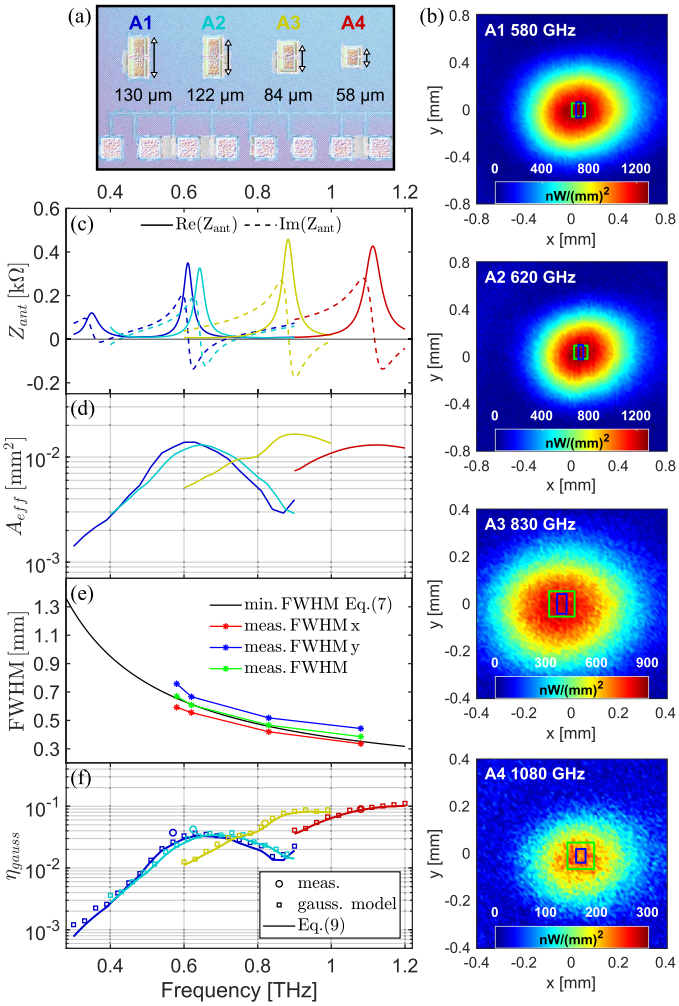

Fig. 2. (a) Top-view micrograph of the array of four detectors (A1–A4) showing the rectangular patch antennas; the corresponding patch lengths are listed. All patches have the same width of 40 μm and height of 8.41 μm above the ground-plane. (b) Direct measurement of the Gaussian beam intensity profile $I_{\text{gauss}}(x, y)$ obtained close to the resonant frequencies of the patch antennas A1–A4. The physical dimensions ($L_{\text{patch}} \cdot W_{\text{patch}}$) of each patch are indicated as blue rectangles, while the simulated effective area A_{eff} is shown in green. (c) Simulated real (solid line) and imaginary part (dashed line) of the antenna impedance Z_{ant} and (d) effective area A_{eff} obtained from EM wave simulations (CST Studio Suite). (e) Extracted FWHM in x (red), y (blue) and estimated mean FWHM (green) of the Gaussian beam intensity profile measured in the focal point of a 2" OAP mirror as presented in (b). The black solid line shows the calculated minimum FWHM from (7) for $d_L = 30$ mm and $f_L = 50.8$ mm. (f) Antenna Gaussian beam coupling efficiency η_{gauss} for each detector (A1–A4) extracted from direct measurements of the Gaussian beam intensity profile (open dots). In addition we present η_{gauss} for arbitrary frequencies assuming (i) an ideal Gaussian beam intensity profile (open squares) and (ii) solving (9) numerically (solid lines). In both cases the FWHM of the Gaussian beam is determined from (7) [as shown as black line in (e)].

[2]In this work, we aim to model explicitly the optical responsivity of the detectors. One distinguishes between *optical* and *cross-sectional* responsivity and NEP [25]. The cross-sectional responsivity is employed if the antenna cross-section is smaller than the beam size. It is calculated as the optical responsivity multiplied by the ratio of the (measured or calculated) beam cross-sectional area at the antenna to the (calculated) antenna cross-sectional area [38].

IV. Power Coupling Theory

For a proper comparison of the simulated optical voltage responsivity with the measured one to be addressed later, the electrical THz input power $P_{\text{in,t}}^{\text{el}}$ at the source transistor terminal (here for source coupling conditions) has to be estimated. For this purpose, we need to consider multiple losses suffered by the incoming radiation before it is converted into the electrical input signal. $P_{\text{in}}^{\text{op}}$ denotes the power of the incoming THz beam directly before the passivation layer. The electric power $P_{\text{in,ant}}^{\text{el}}$, which one obtains from this optical power at the antenna is calculated in the following way:

$$P_{\text{in,ant}}^{\text{el}} = \eta_{\text{op}} \cdot \eta_{\text{scat}} \cdot \eta_{\text{gauss}}(\nu) \cdot P_{\text{in}}^{\text{op}}\,. \tag{4}$$

Here, η_{op} takes into account all possible optical losses of the incident THz radiation on the path from the source to the detector, which are not considered by the electromagnetic (EM) wave simulations. For example absorption and reflection losses associated with the substrate and a lens, which may be attached to it [25], [39]. In this work, we set $\eta_{\text{op}} = 1$, since the incident THz light is coupled directly from free space to the antenna as indicated in Fig. 1(b), neither passing through a substrate nor a substrate/superstrate lens (backside illumination is obstructed by the ground plane). η_{scat} represents the absorption efficiency of the antenna. It includes the residual scattering losses that occur in a receiving antenna element even in case of a perfectly matched load. For large planar antennas it is known to be $\eta_{\text{scat}} \approx 0.5$ [38], [40]. The final loss factor is the frequency-dependent Gaussian beam coupling efficiency $\eta_{\text{gauss}}(\nu)$. From a geometrical point of view, $\eta_{\text{gauss}}(\nu)$ considers collection losses resulting from the discrepancy between the spatial extension of the incident Gaussian beam's intensity profile, given by [41]

$$I_{\text{gauss}}(r,\varphi) = I_0 \cdot \exp\left(-\frac{k_0}{z_R} \cdot r^2\right) \tag{5}$$

and the effective area of the antenna [42]

$$A_{\text{eff}} = \frac{\lambda_0{}^2}{4\pi} \cdot G = \frac{\lambda_0{}^2}{4\pi} \cdot \epsilon_{\text{ant}} \cdot D\,. \tag{6}$$

Here, $z_R = \frac{\pi\nu}{4c_0} \cdot D_{\text{f}}{}^2$ is the Rayleigh range and $k_0 = \frac{2\pi}{\lambda_0} = \frac{2\pi\nu}{c_0}$ the wave vector in free-space with speed of light in vacuum c_0. I_0 denotes the intensity in the center of the Gaussian beam. D_{f} represents the minimum $1/e^2$ Gaussian beam diameter

$$D_{\text{f}} = \frac{\sqrt{2} \cdot \text{FWHM}}{\sqrt{\ln(2)}} = \frac{4 \cdot f_L \cdot c_0}{d_L \cdot \pi \cdot \nu} \tag{7}$$

where d_L is the diameter of the collimated optical beam before the focusing element, FWHM is the full width at half maximum (FWHM) of the indicent gaussian beam intensity profile, and f_L is the focal length of the focusing element (in this work an OAP mirror with $f_L = 2" = 50.8$ mm). The total incident THz power is distributed over $I_{\text{gauss}}(r,\varphi)$ such that

$$\begin{aligned} P_{\text{gauss}} = P_{\text{in}}^{\text{op}} &= \int_A I_{\text{gauss}}(r,\varphi)\,\text{dA} \\ &= \int_0^{\infty}\int_0^{2\pi} r \cdot I_{\text{gauss}}(r,\varphi)\,\text{d}\varphi\text{d}r \\ &= 2\pi \cdot \left[1 - \exp\left(-\alpha r^2\right)\right]_0^{\infty} = \frac{I_0\pi}{\alpha} \end{aligned} \tag{8}$$

with $\alpha = \frac{k_0}{z_R} = \frac{8}{D_{\text{f}}{}^2} = \frac{4\cdot\ln(2)}{\text{FWHM}^2}$. A_{eff} of the receiving antenna element is determined in the direction of maximum gain G.[3] ϵ_{ant} is the antenna efficiency and D the antenna directivity. Both, A_{eff} and ϵ_{ant}, can be obtained from EM simulations [CST Studio Suite, shown in Fig. 2(d)] or from direct measurements (e.g., absolute gain methods or gain transfer methods). For more details about the different methods to estimate the effective area of a THz detector, we refer to [38]. Our EM wave simulations take the full 3-D structure of the Si CMOS TeraFET into account [i.e., all structures shown in the cross-sectional view of Fig. 1(b)]. This includes the vias from the antenna to the transistor and the ground-plane, the surrounding metallization, the different dielectric layers and the passivation layer. The lumped element port is placed at the position of the transistor. In general, the EM wave simulations of $\epsilon_{\text{ant}}(\nu)$ and thus also of $\eta_{\text{gauss}}(\nu)$ consider both conduction losses of the metallization and possible dielectric losses due to the surrounding dielectric layers. Consistent with the real device, the metallization is simulated as lossy copper, so conduction losses are considered in our simulations. Dielectric losses are not considered here because the dielectric layers are made of insulator materials with zero loss tangent.

We want to clarify that the Gaussian beam coupling efficiency $\eta_{\text{gauss}}(\nu)$ is closely related but not identical to the *gaussicity* [43]—a quantity typically employed for substrate-lens-assisted antennas. These typically are configurations, where a dielectric lens (e.g., hyperhemispherical silicon lens) is placed onto the detector's substrate to enhance the Gaussian beam coupling efficiency under backside illumination conditions [20], [43], [44]. The gaussicity can be estimated from the overlap integral of the normalized simulated antenna pattern and the best focused Gaussian beam in the angular domain [39], [43]. This calculation imposes that the effective area of the antenna is larger than (or of the same size as) the Gaussian beam diameter at the position of the antenna plane (after the dielectric lens and the substrate).

In this work, we determine $\eta_{\text{gauss}}(\nu)$ for free-space optical coupling conditions, where the latter condition is not fulfilled. In the following, we assume that the detector is positioned in the focal point of a focusing element, such as an OAP mirror [see Fig. 6(a) in Appendix A] and that the evolution of the optical beam in the experiment can be treated on basis of Gaussian beam theory [41]. Under these circumstances $\eta_{\text{gauss}}(\nu)$ can be calculated for arbitrary frequencies from

$$\begin{aligned} \eta_{\text{gauss}}(\nu) &= \frac{P_{\text{ant}}}{P_{\text{gauss}}} = 1 - \frac{4\beta(\nu)}{\pi} \approx \ln(2) \cdot \frac{\text{A}_{\text{eff}}(\nu)}{\text{A}_{\text{spot}}(\nu)} \\ \beta(\nu) &= \int_0^{\frac{\pi}{4}} \exp\left(-\frac{\ln(2) \cdot \text{A}_{\text{eff}}(\nu)}{\text{FWHM}(\nu)^2} \cdot \frac{1}{\cos^2(\varphi)}\right) \text{d}\varphi \end{aligned} \tag{9}$$

where $\text{FWHM} = \sqrt{\ln(2)/2} \cdot \text{D}_{\text{f}}$ is the frequency-dependent minimum FWHM of the incident Gaussian beam given in the antenna plane (in focal point of the OAP mirror) and $A_{\text{spot}} = \pi \cdot (\text{FWHM}/2)^2$ is the spot size of the beam. Note that the integral for $\beta(\nu)$ has no analytical solution and needs to be solved numerically. However, we find that β can be

[3] A rectangular patch excited in its fundamental mode has a maximum gain in the direction perpendicular to the antenna plane ($\Phi = 0°$). Based on our experimental setup (see Appendix A) we assume perfect perpendicular illumination of the optical beam to the antenna plane to estimate the effective area.

approximated by $\beta \approx \pi/4 - \ln(2) \cdot \mathrm{A_{eff}}/\mathrm{A_{spot}}$, which leads to $\eta_{\mathrm{gauss}} \approx \ln(2) \cdot \mathrm{A_{eff}}/\mathrm{A_{spot}}$. For details on the derivation of the equation set (9), we refer to Appendix B.

Precise knowledge of d_L is therefore required to determine the Gaussian beam intensity profile at the detector position. For this purpose, we estimate the FWHM (or D_{f}) at the focal point of the OAP mirror by direct measurements of the Gaussian beam intensity profile $I_{\mathrm{gauss}}(x, y)$ using an automated X–Y micrometer translation stage as shown in Fig. 2(b) at the respective resonant frequency of each detector A1–A4. We want to emphasize that $I_{\mathrm{gauss}}(x, y)$ may have to be de-embedded when using highly directional antennas with a narrow beamwidth. The 3-db beamwidth (angular width) of the patch antennas in this work is roughly 90° over a wide range of frequencies. From $I_{\mathrm{gauss}}(x, y)$ we determine the FWHM of the Gaussian distribution alongside X (shown as red line) and Y (shown as green line) using a Gaussian fit model [see Fig. 2(e)]. Then, the mean FWHM can be obtained from $\mathrm{FWHM} = \sqrt{\mathrm{FWHM_x} \cdot \mathrm{FWHM_y}}$ (shown as green line). Consequently, we take the observed frequency roll-off of the measured FWHM to define d_L in our measurement system. Best agreement with direct measurements of the FWHM is observed for $d_L = 30$ mm [calculated from (7), shown as black solid line in Fig. 2(e)].

In Fig. 2(f) we plot the calculated Gaussian beam coupling efficiency $\eta_{\mathrm{gauss}}(\nu)$ obtained from the numerical solution of (9) for each patch antenna (A1–A4) taking the simulated effective areas A_{eff} and the experimentally determined minimum FWHM into account. Besides that, we compare the solution of (9) with values of η_{gauss} obtained from the direct evaluation of the numerical area integral for P_{ant} [see (13) in Appendix A] and P_{gauss} [see (8)] using 1) the measured and 2) an ideal symmetric Gaussian beam intensity profile $I_{\mathrm{gauss}}(x, y)$. The latter is determined from the minimum FWHM [see (7)] at the respective frequencies. From Fig. 2(f), even for the A3 and A4 with larger effective antenna area, only about 10% of $P_{\mathrm{in}}^{\mathrm{op}}$ can be coupled into the antenna element in the best case. Finally, the electrical THz input power at the source transistor terminal $P_{\mathrm{in,t}}^{\mathrm{el}}$ [see Fig. 1(a)] is obtained from [13], [20], [25]

$$\begin{aligned} P_{\mathrm{in,t}}^{\mathrm{el}} &= \eta_m(\nu) \cdot P_{\mathrm{in,ant}}^{\mathrm{el}} \\ &= \frac{4 \cdot \mathrm{Re}[\mathrm{Z_{ant}}] \cdot \mathrm{Re}[\mathrm{Z_t}]}{|Z_{\mathrm{ant}} + Z_t|^2} \cdot P_{\mathrm{in,ant}}^{\mathrm{el}} \end{aligned} \tag{10}$$

where $\eta_m(\nu)$ accounts for the impedance mismatch of the antenna impedance $Z_{\mathrm{ant}}(\nu)$ [see Fig. 2(c)] to the transistor channel impedance $Z_t(\nu)$. Best electrical power coupling to the transistor is ensured whenever conjugate impedance matching conditions are present $Z_{\mathrm{ant}} = Z_t^*$. Note, that impedance mismatch effects ($\eta_m(\nu)$) are inherently embedded in the circuit simulation software ADS (e.g., by taking a power source at a certain frequency with complex impedance) and therefore, for the simulations presented here, we use $P_{\mathrm{in,ant}}^{\mathrm{el}}$ as THz power input parameter. Besides the simulated antenna parameters $Z_{\mathrm{ant}}(\nu)$, $A_{\mathrm{eff}}(\nu)$ as well as the Gaussian beam coupling efficiency $\eta_{\mathrm{gauss}}(\nu)$ all other unknown input simulation parameters, in case of ADS-HDM, are obtained from dc drain-to-source resistance (R_{DS}) measurements. The measured resistance curves are fitted to a simple serial resistance model for the MOSFET channel, which is based on the UCCM. The extracted simulation parameters are given in Table I.[4]

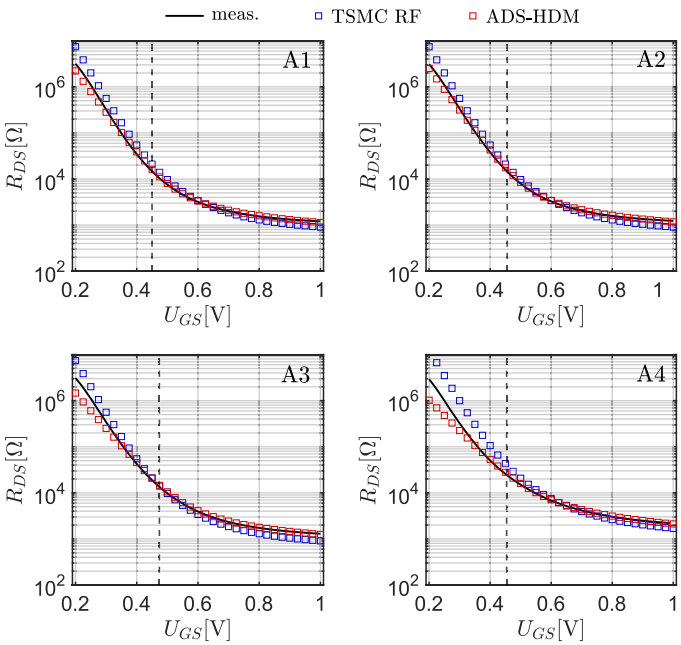

Fig. 3. Comparison of the measured dc drain-to-source resistance (black line) with simulations obtained from TSMC RF (blue open squares) and ADS-HDM (red open squares) for the different Si CMOS TeraFETs (A1-A4). U_{DS} is set to 10 mV for all measurements and simulations. The dashed vertical line represents the extracted U_T for the respective devices using a fit model based on the UCCM (see Table I). For both models we assume a fixed residual resistance of $R_{p,\mathrm{ext}} = 300\ \Omega$ for a short-circuit protection FET, which is connected in series with the drain electrode of all respective transistors.

V. Simulations and Comparison With Measurements

In order to validate the implementation technique and the fitting routine discussed previously we compared the simulated R_{DS} as a function of U_{GS} with measurements. In Fig. 3, R_{DS} is shown for TSMC RF and ADS-HDM together with the respective measured data for a fixed drain-to-source voltage of $U_{\mathrm{DS}} = 10$ mV. We observe good agreement between the ADS-HDM and data, which is a direct consequence of the specific simulation parameter extraction performed for each device separately (see Table I). Contrary TSMC RF exhibits only near-quantitative agreement with data close to U_T. In the inversion regime ($U_{GS} > U_T$) the measured R_{DS} are slightly higher than predicted by TSMC RF. To the best of the authors' knowledge, the discrepancy originates from globalized simulation parameters of the TSMC RF foundry model. These globalized simulation parameters are only adapted depending on the CMOS fabrication process (here CLN65LP, type 1.2V_mLow_Vt_MOS) and the device dimensions (length and width of the channel). Therefore, the foundry model cannot account for possible variations (e.g., due to imperfections, defects, etc.,) of the electrostatic properties within a foundry fabrication run. A comparison of the frequency-dependent measured optical voltage responsivity (top panels)

[4]Note that each detector is connected in series to a different short-circuit protection FET for which we assumed $R_{p,\mathrm{ext}} = 300\ \Omega$. The exact residual resistance of the protection FET is not known to us and might vary between the devices. This can influence the extracted values for R_C.

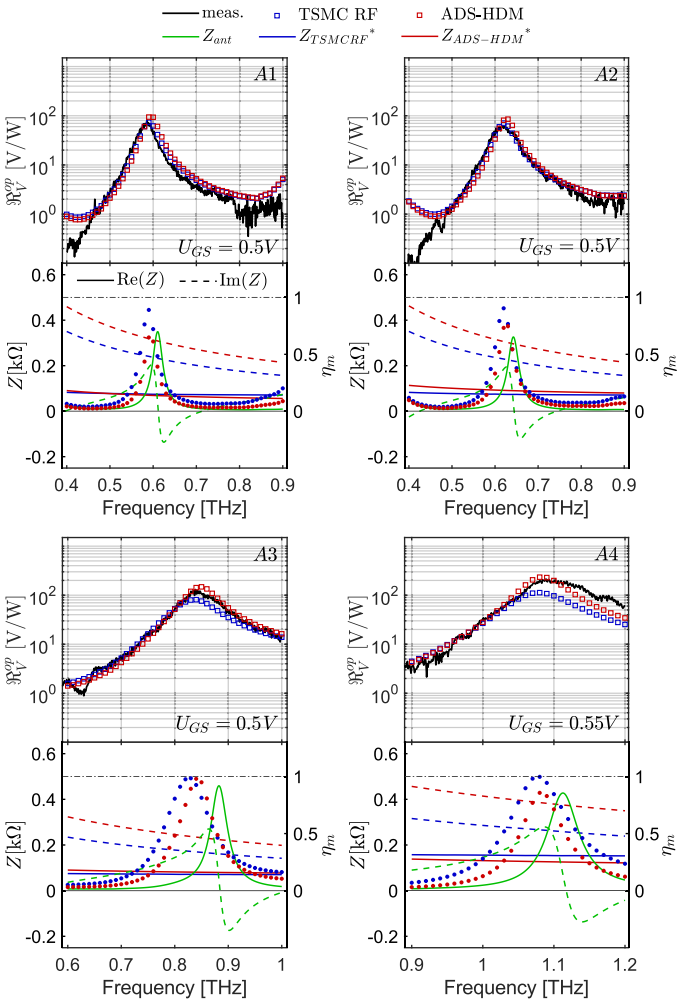

Fig. 4. Top panels: Comparison of the measured frequency-dependent optical voltage responsivity (black line) with simulations using TSMC RF (blue open squares) and ADS-HDM (red open squares) for devices A1–A4. Bottom panels: Comparison of the simulated frequency-dependent real (solid lines) and imaginary (dashed lines) antenna impedance Z_{ant} (green) with corresponding simulations of the complex conjugate transistor channel impedance $Z_t{}^*$ using TSMC RF (blue) and ADS-HDM (red) for the different Si CMOS TeraFET devices. Estimated impedance mismatch factor η_m (dots, right axis) is calculated from (10) for TSMC RF (blue) and ADS-HDM (red).

of devices A1–A4 with the respective simulations—TSMC RF and ADS-HDM—can be seen in Fig. 4. The final unknown simulation parameter of the ADS-HDM—the total parasitic capacitance per micron channel width $C_{ov+fr,W^{-1}}$, which includes the overlap C_{ov} and fringe C_{fr} capacitances—is determined from the comparison of the measured responsivity roll-off of the detector characterized at the highest THz frequencies (A4) with the respective ADS-HDM simulations. Best agreement is found for $C_{\text{ov}+fr,W^{-1}} = 0.75\,\text{fF}/\mu\text{m}$. Similar values have been reported for Si CMOS TeraFETs manufactured with the 150-nm technology by TSMC [13]. Besides that, in simulations of the detector voltage response ΔU_{DS}, the calculation of the dc readout is performed against an effective loading impedance $|Z_L| = |(1/R_{\text{in}} + i \cdot 2\pi f_{\text{mod}} C_L)^{-1}| \approx 440\text{k}\Omega$ [45], taking into account the lock-in amplifier's input impedance R_{in} (10 MΩ) and the effective capacitance of the cable ($C_L = 0.5\,\text{m} \cdot 0.95\,\text{pF/m}$).

We obtain a near-quantitative agreement between both models and measurements at low THz frequencies (Device A1 and A2). Both models predict magnitude, peak position and the roll-off of the measured signal quantitatively. Only far away from the peak (at 0.4 THz for A1 and A2) we observe a discrepancy between data and simulations. As presented in Fig. 2(c) the EM wave simulations of the antenna impedances Z_{ant} suggest an additional antenna resonance at ~ 0.35 THz, which is not observed in the THz characterization measurements. At higher THz frequencies (Device A3 and A4) the predicted peak position and magnitude of the optical voltage responsivity of both models starts to differ. The observed divergence can be related mainly to different predicted losses due to imperfect conjugate impedance matching ($Z_{\text{ant}} \neq Z_t^*$) between Z_{ant} and Z_t. The latter is determined by either TSMC RF or, in case of ADS-HDM, by the hydrodynamic transport equations [see (1)] together with the UCCM [see (2)]. In the bottom panels of Fig. 4 the real part and imaginary part of the simulated complex conjugate transistor channel impedance $Z_t{}^*$ is depicted together with Z_{ant} for each device. In addition we show the calculated impedance mismatch factor η_m [(10), shown as dots, right axis]. Both models suggest that—especially in case of device A3—perfect conjugate impedance matching ($\eta_m \sim 1$) is reached. Remarkably both models predict very similar Z_t. Despite the fact that TSMC RF has not being adapted specifically for the THz frequency range, it exhibits good agreement with measurements and with ADS-HDM. In addition to the frequency-dependent measurements we also measured and simulated the optical voltage responsivity $\mathcal{R}_V^{\text{op}}$ as a function of gate voltage U_{GS}. In Fig. 5(a), we compare the measured optical voltage responsivity of devices A1 to A4 with the results of simulations with ADS-HDM and the TSMC RF for fixed excitation frequencies. Again, we observe good agreement between both models and measurements. Best agreement is obtained in the inversion regime above U_T (marked as vertical dashed line) of the respective transistor, while agreement gets worse below U_T, where $\mathcal{R}_V^{\text{op}}(U_{GS})$ peaks. The deviations are attributed to unknown details of power-coupling and U_{GS}-dependent impedance matching. In addition to results for the full-fledged ADS-HDM, we also plot the predicted purely resistive-mixing response of the transistor, where the diffusive and plasmonic terms of the HDM are neglected and only the low-frequency limit is considered ($\partial_t j \ll j/\tau_p$), such that (1b) is reduced to $j = \sigma \cdot E_x$, with the conductivity $\sigma = (q^2 \tau_p n)/m^*$. The difference between the full ADS-HDM and the purely resistive self-mixing model increases with frequency. The responsivity as predicted by the full model is larger than that of the purely resistive mixing, albeit not by a fixed factor for all values of U_{GS}. The maximal difference reaches values of about 20% for device A4 at 1070 GHz and $U_{GS} = 0.4$ V. This increase is evidence that diffusive and plasmonic features cannot be neglected as the frequency rises. Their influence, however, does not become dominant up to the highest frequencies of our studies, and an approximative treatment of rectification by purely resistive mixing yields fair results.

The presented results of measurements and simulations of the optical voltage responsivity have only considered the measured detector response with respect to the available optical THz input power $P_{\text{in}}^{\text{op}}$. For a detector *sensitivity*, noise contributions to the detected signal must be taken into account. The most important

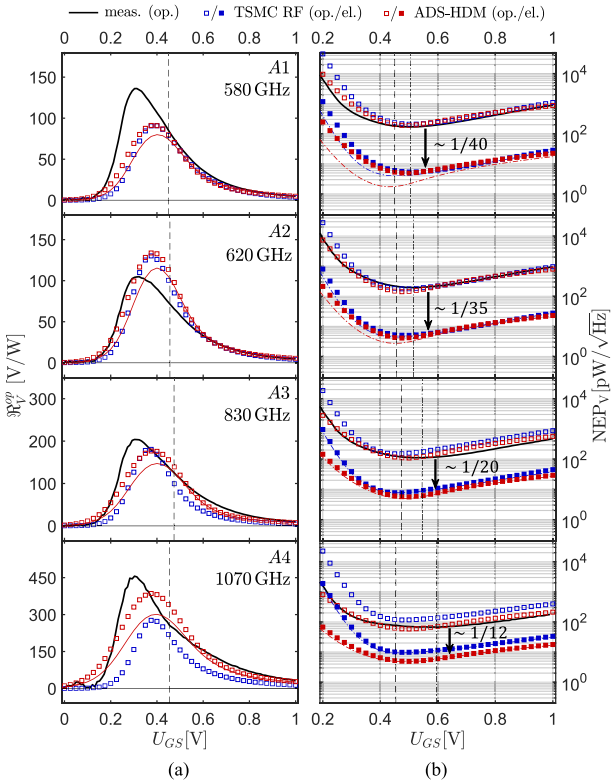

Fig. 5. Left panels: (a) Comparison of the measured voltage-dependent optical responsivity $\mathcal{R}_V^{\text{op}}$ (black line) at constant excitation frequency with corresponding simulations obtained from TSMC RF (blue open squares) and ADS-HDM (red open squares) for A1–A4. The vertical dashed line represents the extracted U_T from R_{DS} measurements in case of the ADS-HDM (see Table I). The pure resistive self-mixing detector response predicted by the ADS-HDM is plotted as red line. Right panels: (b) Comparison of the measured optical voltage-dependent noise-equivalent power (NEP) ($\text{NEP}_{\text{V}}^{\text{op}}$) (black line) at constant excitation frequency with corresponding simulations using the TSMC RF foundry model (blue open squares) and our in-house tool ADS-HDM (red open squares) for the different Si CMOS TeraFET device. The vertical dashed-dotted line represents minimum $\text{NEP}_{\text{V}}^{\text{op}}$ of the respective devices. TSMC RF (blue filled squares) and ADS-HDM (red filled squares) simulations of the voltage-dependent electrical NEP ($\text{NEP}_{\text{V}}^{\text{el}}$) with regards to the maximum available power delivered from the antenna $P_{\text{in,ant}}^{\text{el}}$. In addition, the simulated electrical NEP calculated with regards to the available power at the source transistor terminal $P_{\text{in,t}}^{\text{el}}$ is depicted for TSMC RF (blue dashed line) and ADS-HDM (red dashed line).

figure of merit in this context is the noise-equivalent power (NEP). The NEP is defined as the ratio of the detectors voltage or current noise spectral density (V_N or I_N) in a 1 Hz bandwidth (Δf) and the detectors voltage or current responsivity, respectively. It can be defined with regards to the optical or electrical detector responsivity ($\mathcal{R}_V^{op}$ or $\mathcal{R}_V^{el}$). For measurements of the voltage response we have

$$\text{NEP}_{\text{V}}^{\text{op}} = \frac{V_N}{\mathcal{R}_V^{\text{op}}}$$
$$\text{NEP}_{\text{V}}^{\text{el}} = \frac{V_N}{\mathcal{R}_V^{\text{el}}} \tag{11}$$

where the voltage noise spectral density V_N, in case of zero drain-to-source bias ($U_{DS} = 0$ V) during THz detection operation, is dominated by Johnson—Nyquist (thermal) noise, such that $V_N = \sqrt{4k_B T R_{DS} \Delta f}$ [16], [46]. This assumption is based on noise characterization measurements of Si CMOS TeraFETs

TABLE II
MEASURED MINIMUM $\text{NEP}_{\text{V}}^{\text{op}}$ IN pW/$\sqrt{\text{Hz}}$ AT RESPECTIVE GATE VOLTAGES U_{GS} FOR THE DETECTORS A1–A4 AS WELL AS SIMULATED VALUES OBTAINED FROM TSMC RF AND ADS-HDM FOR $\text{NEP}_{\text{V}}^{\text{op}}$ (OP.) AND $\text{NEP}_{\text{V}}^{\text{el}}$ (EL.) WITH REGARDS TO $P_{\text{IN,ANT}}^{\text{EL}}$

Device	A1	A2	A3	A4
Frequency	580 GHz	620 GHz	830 GHz	1070 GHz
U_{GS}	0.5 V	0.52 V	0.55 V	0.6 V
measured	169.9 (op.)	194.7 (op.)	111 (op.)	67.17 (op.)
TSMC RF	208.2 (op.)	183.3 (op.)	180.6 (op.)	137.74 (op.)
	5.25 (el.)	5.27 (el.)	9.3 (el.)	11.57 (el.)
ADS-HDM	189.9 (op.)	155 (op.)	121.5 (op.)	71.42 (op.)
	4.93 (el.)	4.46 (el.)	6.25 (el.)	6 (el.)

manufactured by TSMC's 90-nm technology [16]. In Fig. 5(b) we present a comparison of the measured optical NEP with simulations obtained by the TSMC RF and the ADS-HDM. Both models correctly predict the overall magnitude and gate voltage dependency of the measured $\text{NEP}_{\text{V}}^{\text{op}}$ close and above the U_T. Below threshold and at higher THz excitation frequencies (A3 and A4) the ADS-HDM achieves better comparability with data. In order to show possible improvements of the detector performance (e.g., by enhancing the Gaussian beam coupling efficiency η_{gauss} or reducing the back-scattering effect of the antenna) we present simulations of the electrical $\text{NEP}_{\text{V}}^{\text{el}}$, which represents the intrinsic lower limit of the detector sensitivity. We perform this calculation for two cases, where the electrical responsivity is referred 1) to the available power originating from the antenna element $\mathcal{R}_V^{\text{el}} = \Delta U_{\text{DS}}/P_{\text{in,ant}}^{\text{el}}$ and 2) to available power at the Source transistor terminal $\mathcal{R}_V^{el} = \Delta U_{\text{DS}}/P_{\text{in,t}}^{\text{el}}$. In the latter impedance mismatch losses η_m are excluded. These losses play a more dominant role at lower THz frequencies, where the device impedance Z_t changes more strongly with applied gate voltage. As already indicated by the estimated values of η_{gauss} [see Fig. 2(f)] and also visible in Fig. 5(b) there is more room for improvements of the detector sensitivity for A1 and A2—with respective small effective antennas areas [see Fig. 2(d)] - then for A3 and A4. For example, if η_{gauss} is increased to ~ 1 by reducing the FWHM of the Gaussian beam intensity profile in the antenna plane using common methods, such as dielectric lenses (placed here on the patch antenna), one can expect that the detector performance increases by a factor of 40 for A1 and 12 for A4. In Table II the best determined optical NEPs for the respective detectors A1–A4 are shown together with the predictions by the TSMC RF and the ADS-HDM at the respective frequencies and gate voltages. In addition we present the simulated electrical NEP (with regards to the $P_{\text{in,ant}}^{\text{el}}$) of the respective devices at the same frequency and gate voltage conditions. The simulations suggest that a minimum NEP of $5 - 6\,\text{pW}/\sqrt{\text{Hz}}$ could be achieved at room temperature in ideal optical coupling conditions ($\eta_{\text{op}} = 1$, $\eta_{\text{gauss}} = 1$, and $\eta_{\text{scat}} = 1$) and $10 - 12\,\text{pW}/\sqrt{\text{Hz}}$ if the backscattering effect of the antenna is taken into account ($\eta_{\text{op}} = 1$, $\eta_{\text{gauss}} = 1$, and $\eta_{\text{scat}} = 0.5$). This in close agreement to the purely analytical calculations of the electrical NEP for 150-nm Si CMOS TeraFETs as presented in [13].

VI. CONCLUSION

In summary, the detector voltage responsivity and sensitivity of four 65-nm Si CMOS TeraFETs in the THz frequency range

of 0.4 and 1.2 THz and the gate voltage range of 0 to 1 V were investigated in detail using two transistor transport models—the TSMC RF foundry model and our in-house ADS-HDM circuit implementation. The THz characterization measurements were performed under nitrogen atmosphere and the accurate peak-to-peak response of our detectors was determined from time-domain data acquisitions in order to ensure a suitable database for both models. The amount of THz power injected into the transistor terminals by the Gaussian beam via the antenna was calculated based on geometric constraints. A near-quantitative agreement between model and experiment was observed over a wide range of THz excitation frequencies and gate voltages. The simulations indicate that the 65-nm Si CMOS TeraFETs perform close to perfect conjugate impedance matching and further improvement of their detector performance down to $\sim 10\,\mathrm{pW}/\sqrt{\mathrm{Hz}}$ at room temperature can be expected if the efficiency of Gaussian beam coupling is improved. By comparing the two models with each other and with experimental I/V and THz characterization, we find that the TSMC RF foundry model is applicable beyond its actual design frequency range for 5G communications and 110 GHz millimeter-wave applications. It can be used with confidence to make predictions about detector performance in the investigated operating range of our Si CMOS TeraFETs up to 1.2 THz. However, the experimental data of A3 and A4 and their comparison with the simulations suggest that the TSMC RF model may lose its validity at frequencies above 1.2 THz at which the plasmonic mixing terms in (1b) are likely to begin to dominate the device response. Our work extends recent advances in compact SPICE circuit modeling of Si MOSFETs in the THz frequency range [35] by two more simulation approaches. In this work, we compare our simulations directly with experimental data and achieve near-quantitative agreement over a wide operating range. We conclude that both models can be used for modeling and designing MOSFET integrated circuits for operating frequencies of at least 1.2 THz (of special interest for 6G communications, THz imaging, biomedical diagnostics, etc). Finally, it is worth to mention that the ADS-HDM can be adapted to several key material technologies in the THz research field, such as graphene, AlGaN/GaN- (as shown in [21]) and AlGaAs/GaAs HEMTs, as the governing hydrodynamic transport equations only need to be coupled to an charge control model suitable for the respective material technology.

Appendix A
Lock-in Amplifier Correction Factor - Toptica TeraScan 1550

In Fig. 6(a), we sketch the measurement setup used to gather the data in this work. The Si CMOS TeraFETs are characterized using the lock-in technique (Ametek DSP 7265) with an electronically modulated InGaAs photomixer emitter (Toptica TeraScan 1550) @ $f_{\mathrm{mod}} = 7.62$ kHz (indicated as blue line). Alignment of the detectors was performed in xyz to guarantee the correct position in the focal point of the final OAP mirror (diameter: 2”). From time-domain acquisitions of the detector signal (red line), we determined the lock-in correction factor α_{LIA} via

$$\alpha_{LIA,\mathrm{corr}} = \frac{\mathrm{Pk2Pk}(\Delta U_{\mathrm{DS}})}{\mathrm{RMS}(\mathrm{U}_{\mathrm{lock-in,1f_{mod}}})} \tag{12}$$

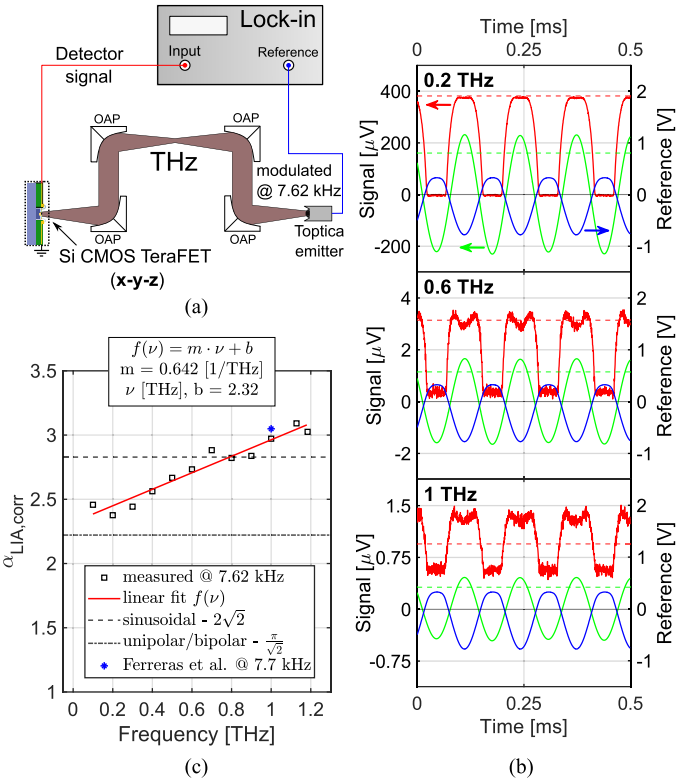

Fig. 6. (a) Schematic drawing of the measurement setup for optical characterization of the Si CMOS TeraFETs. (b) Fundamental component (green) of the detected waveform (red) extracted from time-domain acquisitions (using an oscilloscope) for a single broadband 65-nm Si CMOS TeraFET at 0.2, 0.6 and 1 THz when illuminating the detector with an electronically chopped (reference shown in blue) InGaAs photomixer (Toptica TeraScan 1550). (c) Extracted lock-in correction factor $\alpha_{\mathrm{LIA,corr}}$ as a function of frequency. Calculated values (dashed / dotted lines) for the lock-in correction factor are shown for different types of references/emitter modulations. A reference measurement of $\alpha_{rmLIA,corr}$ at 1 THz measured with the similar Toptica TeraScan 1550 is shown as blue star [39].

as a function of the radiation frequency using a single broadband 65-nm Si CMOS TeraFET (log-spiral antenna).

In Fig. 6(b), the measured detector signal U_{DS} (red line, left axis), the modulation waveform for the Toptica emitter (blue line, right axis) – which serves as the reference for the lock-in amplifier –, and the fundamental component of the measured detector signal $U_{\mathrm{lock-in,1f_{mod}}}$ (green line, left axis) – extracted using Fourier analysis – are presented for three different radiation frequencies (0.2, 0.6 and 1 THz). In addition, the extracted peak-to-peak value (red dashed line), relevant for the detector calibration and sensitivity measurements, as well as the obtained RMS value of the fundamental component (green dashed line), which is measured by the lock-in amplifier after bandpass filtering at $f_{\mathrm{mod}} = 7.62$ kHz, are shown. In Fig. 6(c), we present $\alpha_{\mathrm{LIA,corr}}$ as a function of the radiation frequency. A linear fit is used to determine the observed frequency trend, which is relevant for our simulations and correct predictions of ΔU_{DS}. We speculate that the unexpected frequency dependence of $\alpha_{\mathrm{LIA,corr}}$ is a consequence of frequency-dependent non-linear mixing properties of the Toptica InGaAs photomixer emitter. They manifest, when the photomixer is illuminated by the fiber-coupled dual-color optical beam at different beat-note frequencies $\Delta\nu$ (0.1-1.2 THz). This leads to the observed non-ideal (here

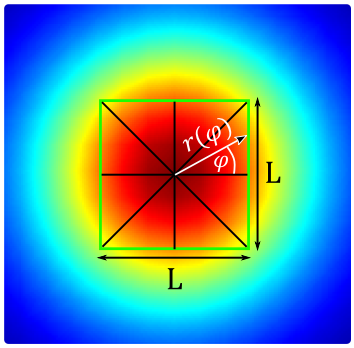

Fig. 7. Sketch for visualizing mathematical steps for the calculation of the Gaussian beam coupling efficiency. The dimensions of the effective area $A_{eff} = L^2$ are indicated as a green square.

non-sinusoidal) modulation of the emitted THz output power and to the change in $\alpha_{\mathrm{LIA,corr}}$ with the beat-note frequency. Further investigations, also at higher frequencies, are needed to clarify the origin of the observed effect.

Appendix B
Gaussian Beam Coupling Efficiency

In order to calculate the total power coupled into the effective area (indicated as green square in Fig. 7) of an arbitrary planar antenna we assume a point symmetry of $I_{\mathrm{gauss}}(x, y)$ to split the calculation into 8 equal triangles as indicated in Fig. 7 (black triangles). Together with the parameterization $r(\varphi) = \frac{L}{2} \cdot \cos\varphi$ we obtain

$$\begin{aligned} P_{\mathrm{ant}} &= \int\int_{A_{eff}} I_{\mathrm{gauss}}(x,y)\,\mathrm{dxdy} \\ &= 8 \cdot \int\int_{A_\Delta} I_{\mathrm{gauss}}(x,y)\,\mathrm{dxdy} \\ &= 8I_0 \cdot \int_0^{\frac{\pi}{4}} \int_0^{r(\varphi)} r \cdot \exp\left(-\alpha r^2\right) \mathrm{d}\varphi\mathrm{d}r \\ &= \frac{4I_0}{\alpha} \cdot \int_0^{\frac{\pi}{4}} \left[1 - \exp\left(\frac{\alpha \cdot L^2}{4} \frac{1}{\cos\varphi^2}\right)\right] \mathrm{d}\varphi \\ &= \frac{I_0}{\alpha} \cdot [\pi - 4\beta]. \end{aligned} \tag{13}$$

With the definition of the Gaussian beam coupling efficiency $\eta_{\mathrm{gauss}} = \frac{P_{\mathrm{ant}}}{P_{\mathrm{gauss}}}$ we finally derive the equation set (9).

References

[1] M. Dyakonov and M. Shur, "Detection, mixing, and frequency multiplication of terahertz radiation by two-dimensional electronic fluid," *IEEE Trans. Electron Devices*, vol. 43, no. 3, pp. 380–387, Mar. 1996.

[2] D. Glaab et al., "Terahertz heterodyne detection with silicon field-effect transistors," *Appl. Phys. Lett.*, vol. 96, no. 4, Jan. 2010, Art. no. 042106, doi: 10.1063/1.3292016.

[3] V. Giliberti et al., "Heterodyne and subharmonic mixing at 0.6 THz in an AlGaAs/InGaAs/AlGaAs heterostructure field effect transistor," *Appl. Phys. Lett.*, vol. 103, no. 9, 2021, Art. no. 093505.

[4] A. Lisauskas, S. Boppel, M. Mundt, V. Krozer, and H. G. Roskos, "Subharmonic mixing with field-effect transistors: Theory and experiment at 639GHz high above f(T)," *IEEE Sensors J.*, vol. 13, no. 1, pp. 124–132, Jan. 2013.

[5] H. Yuan, D. Voss, A. Lisauskas, D. Mundy, and H. G. Roskos, "3D Fourier imaging based on 2D heterodyne detection at THz frequencies," *APL Photon.*, vol. 4, no. 10, 2019, Art. no. 106108.

[6] M. M. Wiecha et al., "Direct nanoscopic observation of plasma waves in the channel of a graphene field-effect transistor," *Nanoscale Devices*, vol. 3, pp. 1717–1724, Mar. 2021.

[7] W. Knap et al., "Field effect transistors for terahertz detection: Physics and first imaging applications," *J. Infrared, Millimeter, Terahertz Waves*, vol. 30, pp. 1319–1337, Aug. 2009, doi: 10.1007/s10762-009-9564-9.

[8] E. Öjefors, U. R. Pfeiffer, A. Lisauskas, and H. G. Roskos, "A 0.65 THz focal-plane array in a quarter-micron CMOS process technology," *IEEE J. Solid-State Circuits*, vol. 44, no. 7, pp. 1968–1976, Jul. 2009. [Online]. Available: https://ieeexplore.ieee.org/lpdocs/epic03/wrapper.htm?arnumber=5109781

[9] A. Lisauskas et al., "Rational design of high-responsivity detectors of terahertz radiation based on distributed self-mixing in silicon field-effect transistors," *J. Appl. Phys.*, vol. 105, no. 11, 2009, Art. no. 114511, doi: 10.1063/1.3140611.

[10] V. V. Popov et al., "High-responsivity terahertz detection by on-chip InGaAs/GaAs field-effect-transistor array," *Appl. Phys. Lett.*, vol. 98, no. 15, Apr. 2011, Art. no. 153504. [Online]. Available: http://scitation.aip.org/content/aip/journal/apl/98/15/10.1063/1.3573825

[11] G. C. Dyer et al., "Enhanced performance of resonant sub-terahertz detection in a plasmonic cavity," *Appl. Phys. Lett.*, vol. 100, no. 8, Feb. 2012, Art. no. 083506. [Online]. Available: http://scitation.aip.org/content/aip/journal/apl/100/8/10.1063/1.3687698

[12] J. D. Sun et al., "Probing and modelling the localized self-mixing in a GaN/AlGaN field-effect terahertz detector," *Appl. Phys. Lett.*, vol. 100, no. 17, 2012, Art. no. 173513.

[13] S. Boppel et al., "CMOS integrated antenna-coupled field-effect transistors for the detection of radiation from 0.2 to 4.3 THz," *IEEE Trans. Microw. Theory Techn.*, vol. 60, no. 12, pp. 3834–3843, Dec. 2012. [Online]. Available: https://ieeexplore.ieee.org/lpdocs/epic03/wrapper.htm?arnumber=6353608

[14] S. Blin et al., "Wireless communication at 310 GHz using GaAs high-electron-mobility transistors for detection," *J. Commun. Netw.*, vol. 15, no. 6, pp. 559–568, 2013.

[15] W. Knap et al., "Nanometer size field effect transistors for terahertz detectors," *Nanotechnol.*, vol. 24, no. 21, 2013, Art. no. 214002. [Online]. Available: http://www.ncbi.nlm.nih.gov/pubmed/23618776

[16] M. Bauer et al., "Antenna-coupled field-effect transistors for multi-spectral terahertz imaging up to 4.25 THz," *Opt. Exp.*, vol. 22, no. 16, pp. 19235–19241, 2014.

[17] J. Grzyb and U. Pfeiffer, "THz direct detector and heterodyne receiver arrays in silicon nanoscale technologies," *J. Infrared, Millimeter, Terahertz Waves*, vol. 36, no. 10, pp. 998–1032, 2015.

[18] J. D. Sun et al., "Passive terahertz imaging detectors based on antenna-coupled high-electron-mobility transistors," *Opt. Exp.*, vol. 28, no. 4, pp. 4911–4920, 2020.

[19] M. Andree, J. Grzyb, R. Jain, B. Heinemann, and U. R. Pfeiffer, "Broadband modeling, analysis, and characterization of SiGe HBT terahertz direct detectors," *IEEE Trans. Microw. Theory Techn.*, vol. 70, no. 2, pp. 1314–1333, Feb. 2022.

[20] K. Ikamas et al., "Broadband terahertz power detectors based on 90-nm silicon CMOS transistors with flat responsivity up to 2.2 THz," *IEEE Electron Device Lett.*, vol. 39, no. 9, pp. 1413–1416, Sep. 2018.

[21] F. Ludwig, M. Bauer, A. Lisauskas, and H. G. Roskos, "Circuit-based hydrodynamic modeling of AlGaN/GaN HEMTs," in *Proc. ESSDERC - 49th Eur. Solid-State Device Res. Conf.*, 2019, pp. 270–273.

[22] M. Dyakonov and M. Shur, "Shallow water analogy for a ballistic field effect transistor: New mechanism of plasma wave generation by DC current," *Phys. Rev. Lett.*, vol. 71, no. 15, pp. 2465–2468, Oct. 1993, doi: 10.1103/PhysRevLett.71.2465.

[23] C. Drexler et al., "Helicity sensitive terahertz radiation detection by field effect transistors," *J. Appl. Phys.*, vol. 111, no. 12, Jun. 2012, Art. no. 124504. [Online]. Available: http://scitation.aip.org/content/aip/journal/jap/111/12/10.1063/1.4729043

[24] S. Boppel et al., "0.25-μm GaN TeraFETs optimized as THz power detectors and intensity-gradient sensors," *IEEE Trans. Terahertz Sci. Technol.*, vol. 6, no. 2, pp. 348–350, Mar. 2016, doi: 10.1109/TTHZ.2016.2520202.

[25] M. Bauer et al., "A high-sensitivity AlGaN/GaN HEMT terahertz detector with integrated broadband bow-tie antenna," *IEEE Trans. Terahertz Sci. Technol.*, vol. 9, no. 4, pp. 430–444, Jul. 2019.

[26] D. A. Bandurin et al., "Resonant terahertz detection using graphene plasmons," *Nature Commun.*, vol. 9, 2018, Art. no. 5392.

[27] A. Soltani et al., "Direct nanoscopic observation of plasma waves in the channel of a graphene field-effect transistor," *Light: Sci. Appl.*, vol. 9, 2020, Art. no. 97.
[28] J. M. Caridad et al., "Room-temperature plasmon-assisted resonant THz detection in single-layer graphene transistors," *Nano Lett.*, vol. 24, pp. 935–942, 2024.
[29] M. Shur, T. Fjeldly, T. Ytterdal, and K. Lee, "Unified MOSFET model," *Solid-State Electron.*, vol. 35, no. 12, pp. 1795–1802, Dec. 1992. [Online]. Available: https://linkinghub.elsevier.com/retrieve/pii/003811019290263C
[30] I. Saad, M. L. P. Tan, M. T. Ahmadi, R. Ismail, and V. K. Arora, "The dependence of saturation velocity on temperature, inversion charge and electric field in a nanoscale mosfet," *Int. J. Nanoelectronics Mater.*, vol. 3, pp. 17–34, 2010.
[31] S. Bhardwaj, N. K. Nahar, and J. L. Volakis, "Numerical modeling of plasma oscillations in 2D electron gas for THz HEMT devices," in *Proc. IEEE Nat. Aerosp. Electron. Conf.*, 2014, pp. 302–303.
[32] C. Jungemann, K. Bittner, and H. G. Brachtendorf, "Simulation of plasma resonances in MOSFETs for THz-signal detection," in *Proc. Joint Int. EUROSOI Workshop Int. Conf. Ultimate Integration Silicon*, 2016, pp. 48–51.
[33] X. Liu and M. Shur, "An efficient TCAD model for TeraFET detectors," in *Proc. IEEE Radio Wireless Symp.*, 2019, pp. 1–4.
[34] T. Linn, K. Bittner, H.G. Brachtendorf, and C. Jungemann, "Simulation of THz oscillations in semiconductor devices based on balance equations," *J. Sci. Comput.*, vol. 85, pp. 1–15, 2020.
[35] X. Liu, T. Ytterdal, V. Y. Kachorovskii, and M. Shur, "Compact terahertz SPICE/ADS model," *IEEE Trans. Electron Devices*, vol. 66, no. 6, pp. 2496–2501, Jun. 2019.
[36] X. Liu, T. Ytterdal, and M. Shur, "Multi-segment TFT compact model for THz applications," *Nanomaterials*, vol. 12, 2022, Art. no. 765.
[37] T. Grasser and S. Selberherr, "Mixed-mode device simulation," *Microelectronics J.*, vol. 31, pp. 873–881, 2000.
[38] E. Javadi et al., "Sensitivity of field-effect transistor-based terahertz detectors," *Sensors*, vol. 21, no. 9, 2021, Art. no. 2909. [Online]. Available: https://www.mdpi.com/1424-8220/21/9/2909
[39] M. Ferreras, D. Cibiraite-Lukenskiene, A. Lisauskas, J. Grajal, and V. Krozer, "Broadband sensing around 1 THz via a novel biquad-antenna-coupled low-NEP detector in CMOS," *IEEE Trans. Terahertz Sci. Technol.*, vol. 11, no. 1, pp. 16–27, Jan. 2021.
[40] J. Andersen and A. Frandsen, "Absorption efficiency of receiving antennas," *IEEE Trans. Antennas Propag.*, vol. 53, no. 9, pp. 2843–289, Sep. 2005.
[41] A. Yariv and P. Yeh, Eds., *Photonics : Optical Electronics in Modern Communications*, (Series The Oxford Series in Electrical and Computer Engineering), vol. 6. New York, NY, USA: Oxford Univ. Press, 2007.
[42] J. L. Volakis, *Antenna Eng. Handbook*, 4th ed., New York, NY, USA: McGraw-Hill, 2007. [Online]. Available: http://accessengineeringlibrary.com/content/book/9780071475747
[43] D. F. Filipovic, S. S. Gearhart, and G. M. Rebeiz, "Double-slot antennas on extended hemispherical and elliptical silicon dielectric lenses," *IEEE Trans. Microw. Theory Techn.*, vol. 41, no. 10, pp. 1738–1749, Oct. 1993.
[44] J. V. Rudd and D. M. Mittleman, "Influence of substrate-lens design in terahertz time-domain spectroscopy," *J. Opt. Soc. Amer. B*, vol. 19, no. 2, pp. 319–329, Feb. 2002. [Online]. Available: https://opg.optica.org/abstract.cfm?URI=josab-19-2-319
[45] M. Sakowicz et al., "Terahertz responsivity of field effect transistors versus their static channel conductivity and loading effects," *J. Appl. Phys.*, vol. 110, no. 5, Sep. 2011, Art. no. 054512, doi: 10.1063/1.3632058.
[46] A. Lisauskas et al., "Terahertz responsivity and low-frequency noise in biased silicon field-effect transistors," *Appl. Phys. Lett.*, vol. 102, no. 15, Apr. 2013, Art. no. 153505. [Online]. Available: http://scitation.aip.org/content/aip/journal/apl/102/15/10.1063/1.4802208

Florian Ludwig received the master's degree in physics in 2018 from Wolfgang Goethe-Universität Frankfurt am Main, Frankfurt, Germany, where he is currently working toward the Ph.D. degree in thermoelectric contributions to electronic transport and THz responsivity of TeraFETs – simulations and experiments with the Ultrafast Spectroscopy and Terahertz Physics Group.

His current research interests include theoretical and experimental studies of plasma wave mixing and photo-thermoelectric effects in field-effect transistors, which are used for THz applications.

Mr. Ludwig was the recipient of the the Philipp-Siedler Preis by the Physikalischer Verein Frankfurt in 2019.

Jakob Holstein received first state examination diploma (M.Ed.) for mathematics and physics upper secondary class teaching profession in 2020 the B.Sc. and M.Sc. degrees in physics in 2021 and 2022, respectively, from the Johann Wolfgang Goethe-University Frankfurt am Main, Frankfurt, Germany, where he is currently working toward the Ph.D. degree in integrated measurement system for gas spectroscopy at 2-5 THz - power detection and heterodyne detection using TeraFETs and THz QCLs with the Ultrafast Spectroscopy and Terahertz Physics Group.

He is working on the realization of integrated TeraFET systems for sensing applications, especially for gas spectroscopy applications, where improvement of THz-power coupling mechanisms play an important role. His research interests include experimental characterization of Si-CMOS and graphene-based TeraFETs.

Anastasiya Krysl received the master's degree in physical and mathematical sciences from the Belarusian State University, Minsk, Belarus, in 2017. She is currently working toward the Ph.D. degree with the research group of Professor Roskos, Wolfgang Goethe-Universität Frankfurt am Main, Frankfurt, Germany.

Her research interests include concentrated around design, modeling, characterization and performance optimization of silicon CMOS TeraFETs.

Alvydas Lisauskas (Member, IEEE) received the diploma in physics from Vilnius University, Vilnius, Lithuania, in 1995, and the Ph.D. degree in electrical noise in colossal magnetoresistors and ferroelectrics from the Royal Institute of Technology, Stockholm, Sweden, in 2001.

In 2002, he was a Postdoctor with the Ultrafast Spectroscopy and Terahertz Physics Group, Goethe University Frankfurt, Frankfurt, Germany, working on novel semiconductor devices for THz applications. Since 2014, he has been a Professor with Vilnius University and a Leading Researcher with the Center for Physical Science and Technology, Vilnius, Lithuania. Since 2019, he has been a Group Leader on Terahertz Electronics with the Center for Terahertz Research and Applications, Institute of High Pressure Physics PAS, Warsaw, Poland. His research interests include terahertz electronics, design and modeling of semiconductor devices, and terahertz imaging techniques.

Hartmut G. Roskos studied Physics from the Technical Universities of Karlsruhe (now Karlsruhe Institute of Technology, KIT) and Munich. He received the diploma degree and the Ph.D. degree, with a thesis on femtosecond spectroscopy in solid-state physics, from the TU Munich, Munuch, Germany, in 1985 and 1989, respectively, and the Habilitation degree from RWTH Aachen, Aachen, Germany, in 1996, with a thesis entitled "Coherent Phenomena in Solid-State Physics Investigated by THz Spectroscopy."

From 1989 to 1991, he was a Postdoctoral Researcher with the labs of Dr. Martin Nuss, Dr. Jagdeep Shah, and Dr. Wayne Knox at AT&T Bell Laboratories, Holmdel, NJ, USA, where he was engaged in research on THz physics and THz photonics. He started a THz research group with the Institute of Semiconductor Electronics, RWTH Aachen, led by Prof. Dr. Heinrich Kurz. Since 1997, he is a Full Professor of Physics with Johann Wolfgang Goethe-Universität, Frankfurt am Main, Frankfurt, Germany, where he is the Head of the Ultrafast Spectroscopy and Terahertz Physics Group. He spent sabbatical semesters with the University of California, Santa Barbara in 2005, Institute of Laser Engineering, Osaka University in 2009 and 2010, and with the Institute of Optics of the University of Rochester, NY, USA, in 2014. In 2009, OC Oerlikon AG awarded his group jointly with the Ferdinand Braun Institute, Berlin, a five-year endowed Professorship for Terahertz Photonics. His research interets include THz physics and photonics, THz imaging, and the time-resolved optical and THz spectroscopy of solid-state materials.